IET Power Electronics

Research Article

IET Journals
The Institution of Engineering and Technology

Fault diagnosis in grid-connected PV NPC inverters by a model-based and data processing combined approach

ISSN 1755-4535
Received on 7th April 2018
Revised 17th March 2019
Accepted on 31st July 2019
doi: 10.1049/iet-pel.2018.5237
www.ietdl.org

José Aagel Pecina Sánchez[1], Daniel U. Campos-Delgado[2] ✉, Diego R. Espinoza-Trejo[1], Andres A. Valdez-Fernández[2], Cristian H. De Angelo[3]

[1]*Coordinación Académica Región Altiplano, Universidad Autónoma de San Luis Potosí, C.P. 78700, San Luis Potosí, Mexico*
[2]*Facultad de Ciencias, Universidad Autónoma de San Luis Potosí, C.P. 78290, San Luis Potosí, Mexico*
[3]*Grupo de Electrónica Aplicada, Universidad Nacional de Río Cuarto – CONICET, Córdoba, Argentina*
✉ *E-mail: ducd@fciencias.uaslp.mx*

Abstract: This study presents a fault detection and isolation (FDI) method for open-circuit faults (OCFs) in the switching devices of a grid-connected neutral-point-clamped (NPC) inverter for photovoltaic (PV) applications. The proposed methodology addresses the fault diagnosis problem by a combined model-based and data processing perspective to study single and simultaneous faults in the NPC inverter. For the model-based scheme, a bank of sliding-mode proportional–integral observers is suggested to estimate the fault profiles under an additive model. Thus, from the estimated fault profiles, and by performing a directional residual evaluation in a fixed reference frame, single and simultaneous fault scenarios can be isolated in the NPC inverter. However, for some fault classes, there is some ambiguity by just the model-based approach that is overcome by employing the average line currents to construct extra fault signatures. The proposed FDI scheme only requires the measurements of line currents and grid voltages in the diagnosis media and can isolate 6×2 single OCFs and 12×4 simultaneous OCFs in the order or lower than a fundamental period of the grid frequency. Our new FDI methodology is validated through experimental data from a practical PV system in a closed-loop grid-connected NPC inverter under single and simultaneous OCF conditions.

1 Introduction

Over the next few years, renewable technologies will play a critical role in the world energy scenario, owing chiefly to the impact of increased global warming from fossil fuel use. Among the renewable alternatives, photovoltaic (PV) technologies represent one of the most important and promising clean energy sources [1]. Currently, the most common technology is grid-connected PV systems [2]. In this technology, a power inverter is essential for system operation. Among the converter topologies for power conditioning reported in the literature, the neutral-point-clamped (NPC) multilevel inverter is of great interest in medium/large grid-connected PV systems due to its lower harmonic distortion in the output voltages [3] and reduced filtering requirement that allows for a compact design in the power conditioning unit. One key aspect in power electronic systems is reliability, mainly for those applications where availability is a critical parameter, and the continuous operation of the system even under fault conditions is mandatory. This is the case of grid-connected PV systems. There are different types of faults that can be developed in a PV system, e.g. PV module failures, DC-link failures, open-circuit faults (OCFs) and short-circuit faults (SCFs), respectively, in the switching devices, sensor and controller faults, and utility network faults. According to Petrone *et al*. [4], several surveys classify the power inverter as the most vulnerable component in a PV system. Indeed, semiconductor power devices and capacitors are considered the most fragile inverter components [5].

Among the aforementioned catastrophic failures in the switching devices of the inverter, the occurrence of a SCF will stop the operation of the system. In fact, by adding electrical protections in the topology of the power inverter, a SCF will have the same effect of an open-circuit fault (OCF) [6]. Meanwhile, an OCF will degrade the efficiency of the system, since the converter can still operate with performance deterioration. Moreover, a critical condition is derived from an OCF in the inverter of a grid-connected PV system, since DC components are injected into the line currents, which can lead to saturation effects in the distribution transformers and inductive loads. This negative effect will be more severe in the case of a simultaneous OCF in the inverter, so a prompt detection of this scenario is mandatory. On the other side, since the number of semiconductor devices in NPC inverters is larger than in conventional full-bridge topologies, the probability of fault occurrence is much higher [7]. Nonetheless, an NPC inverter have sufficient degrees of freedom to reconfigure its architecture just by adding some extra power devices [8]; although its fault tolerant ability will depend on an accurate, and fast detection and isolation of the faulty device, so that the NPC inverter can be reconfigured with respect to its topology or control algorithm to avoid a large performance deterioration.

In the literature, several works have addressed the problem of OCF diagnosis in conventional and NPC inverter topologies, where line currents and output voltages are the most common measurements needed to carry out the fault detection and isolation (FDI) methodologies [9–19]. In [9], the resulting trajectory of the current vector in the *dq*-plane after the Clarke transformation was analysed to diagnose OCFs. In [10], a fault diagnosis strategy was suggested for the NPC back-to-back converter by recognition of the zero-conduction times through the power devices. Mendes *et al*. [11] suggested a new algorithm for OCFs in NPC inverters for induction motor variable speed drives, where the residuals were constructed from the mean values of the line currents and the location of the resulting Park's vector. A scheme based on analogue and digital electronics was proposed in [12], where open and short-circuit fault detection circuits were implemented in the insulated-gate bipolar transistor (IGBT) gate driver with adaptive thresholds. In [13], Jlassi *et al.* presented a model-based FDI algorithm for multiple OCF diagnosis in H-Bridge back-to-back converters applied to permanent-magnet synchronous generator drives for wind turbine systems. Meanwhile, Lee *et al.* [14] suggested a fault tolerant control for OCFs in NPC and T-type rectifiers, where the OCF compensation is performed just by injecting the exact *d*-axis current value to eliminate the current distortion. Caseiro and Mendes introduced in [15] a diagnostic algorithm for single OCF in NPC rectifiers. The FDI method in [15] is based on the rectifier

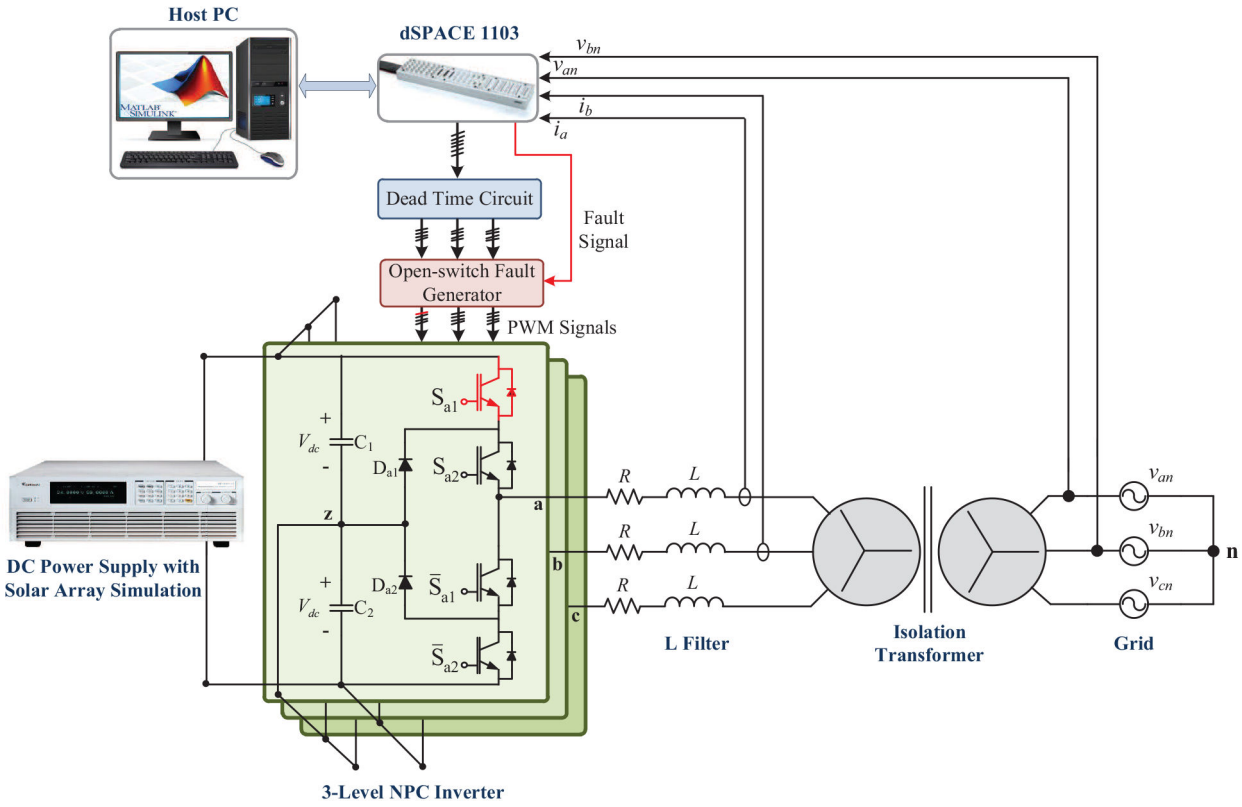

Fig. 1 *PV NPC inverter connected to the utility grid*

pole voltages and the line current behaviour, where the DC-link voltage, the line-to-line grid voltages, and the line currents measurements are required to perform the diagnostic media. In addition, a data processing method to diagnose OCF in power switches and clamping diodes of a NPC inverter was presented [16]. In this case, the information of the dc-link voltage, line currents, and output pole voltages was required for FDI purposes. Likewise, an FDI methodology based on the mean values of the line currents was proposed in [17] for OCF diagnosis in the IGBTs and clamping diodes of a grid-connected NPC inverter. Recently, in [18], a fault-tolerant predictive control strategy was proposed for OCF in the NPC converter of the rotor side for a wind energy conversion system, where the authors introduced an extension of the fault diagnosis algorithm reported in [15]. Meanwhile, in [19], Abdelghani *et al.* presented a fault tolerant scheme for a hybrid converter based on NPC and flying capacitor topologies, where the fault diagnosis scheme relies on a hardware technique that compares the gate signals of the converter and the resulting voltages in the IGBTs.

As previously highlighted, a model-based FDI approach offers significant advantages regarding the ability to identify simultaneous faults and detecting and isolating them promptly [13, 20, 21]. In this context, the main contributions of this work are described next:

- The proposal of a new methodology for FDI in three-phase NPC inverters by considering a combined model-based and data processing approach.
- The model-based algorithm relies on a novel structure of sliding-mode proportional–integral (PI) observers, and on the data processing of the average and instantaneous information of the line currents and grid voltages to isolate the specific faulty switch in the inverter leg.
- The FDI methodology can address both single and simultaneous OCFs in all the power switches of the NPC inverter, such that 6×2 single OCFs and 12×4 simultaneous OCFs can be isolated in the order or lower than a fundamental period of the grid frequency.
- The implementation of our proposed FDI algorithm requires just the measurements of the line currents and grid voltages, which are generally available in the closed-loop control of the NPC inverter [22]. Hence our proposal does not require any other measurement of the system.

In the literature and according to our knowledge, there is no other FDI algorithm with the diagnostic capacity of this proposal without requiring extra measurements and capable of identifying single and simultaneous faults [10–16, 18, 19].

The notation used in this study is described next. Scalars are denoted by italic letters, and vectors and matrices by lower and upper-case bold letters, respectively. $\mathbb{R}$ represents the real numbers, and $\mathbb{R}^-$ and $\mathbb{R}^+$ the subsets of negative and positive real numbers, respectively. $\mathbb{R}^N$ stands for N-dimensional real vectors, and $\mathbb{R}^{N\times M}$ for real matrices of dimensions $N \times M$. For a real vector $\boldsymbol{x}$, the transpose operation is denoted by $\boldsymbol{x}^\top$ and the Euclidean norm by $\| \boldsymbol{x} \|_2 = \sqrt{\boldsymbol{x}^\top \boldsymbol{x}}$. For a full-row rank matrix $\boldsymbol{X} \in \mathbb{R}^{N\times M} (N < M)$, its right-inverse is denoted by $\boldsymbol{X}_r^{-1} \in \mathbb{R}^{M\times N}$; and $\boldsymbol{I}_N$ denotes the identity matrix of order N.

2 NPC inverter system model

Fig. 1 shows the circuit diagram of the studied three-phase grid-connected NPC inverter supplied by a solar array, which can be modelled as a DC voltage source. In the schematic, each phase is connected to the grid through an inductor L in series with a resistor R that models the electrical losses. The OCF condition in the power switching devices of the NPC inverter is triggered by an OCF generator card based on analogue electronics. On the other hand, although grid-connected NPC inverters can operate with transformerless configuration, in this test bench an isolation transformer is employed for safety purposes, and to block the DC components induced in the line currents during the period that the inverter operates under an OCF condition.

The studied multilevel topology considers 12 power switches $(S_{l1}, S_{l2}, S_{l3}, S_{l4}) \forall l \in \{a, b, c\}$, where the midpoint of the DC-link capacitors is defined as the neutral point z. The mathematical model of the NPC inverter is obtained by following a similar approach as in [23], and considering the next assumptions:

A1: All the power switching devices are assumed ideal.

Table 1 Profile directions for each fault class of the NPC inverter and thresholds considered for fault isolation (similar fault profile $f_{\alpha\beta}$ are highlighted)

Fault class	Faulty switches	Unitary vectors		Thresholds		Fault Signatures		
		f_{abc}	$f_{\alpha\beta}$	r_α	r_β	$\mathscr{D}_a$	$\mathscr{D}_b$	$\mathscr{D}_c$
1	(S_{a1} and/or S_{a2})	$[-1,0,0]^\top$	$[-1,0]^\top$	$-1.25 < r_\alpha < -0.75$	$-0.25 < r_\beta < 0.25$	N	Z	Z
2	(S_{a3} and/or S_{a4})	$[1,0,0]^\top$	$[1,0]^\top$	$0.75 < r_\alpha < 1.25$	$-0.25 < r_\beta < 0.25$	P	Z	Z
3	(S_{b1} and/or S_{b2})	$[0,-1,0]^\top$	$[1/2,-\sqrt{3}/2]^\top$	$0.25 < r_\alpha < 0.75$	$-1.1 < r_\beta < -0.6$	Z	N	Z
4	(S_{b3} and/or S_{b4})	$[0,1,0]^\top$	$[-1/2,\sqrt{3}/2]^\top$	$-0.75 < r_\alpha < -0.25$	$0.6 < r_\beta < 1.1$	Z	P	Z
5	(S_{c1} and/or S_{c2})	$[0,0,-1]^\top$	$[1/2,\sqrt{3}/2]^\top$	$0.25 < r_\alpha < 0.75$	$0.6 < r_\beta < 1.1$	Z	Z	N
6	(S_{c3} and/or S_{c4})	$[0,0,1]^\top$	$[-1/2,-\sqrt{3}/2]^\top$	$-0.75 < r_\alpha < -0.25$	$-1.1 < r_\beta < -0.6$	Z	Z	P
7	(S_{a1} and/or S_{a2}) & (S_{b1} and/or S_{b2})	$[-1,-1,0]^\top$	$[-1/2,-\sqrt{3}/2]^\top$	$-0.75 < r_\alpha < -0.25$	$-1.1 < r_\beta < -0.6$	N	N	P
8	(S_{a1} and/or S_{a2}) & (S_{b3} and/or S_{b4})	$[-1,1,0]^\top$	$[-\sqrt{3}/2,1/2]^\top$	$-1.1 < r_\alpha < -0.6$	$0.25 < r_\beta < 0.75$	X	X	X
9	(S_{a1} and/or S_{a2}) & (S_{c1} and/or S_{c2})	$[-1,0,-1]^\top$	$[-1/2,\sqrt{3}/2]^\top$	$-0.75 < r_\alpha < -0.25$	$0.6 < r_\beta < 1.1$	N	P	N
10	(S_{a1} and/or S_{a2}) & (S_{c3} and/or S_{c4})	$[-1,0,1]^\top$	$[-\sqrt{3}/2,-1/2]^\top$	$-1.1 < r_\alpha < -0.6$	$-0.75 < r_\beta < -0.25$	X	X	X
11	(S_{c3} and/or S_{c4}) & (S_{a3} and/or S_{a4})	$[1,0,1]^\top$	$[1/2,-\sqrt{3}/2]^\top$	$0.25 < r_\alpha < 0.75$	$-1.1 < r_\beta < -0.6$	P	N	P
12	(S_{c3} and/or S_{c4}) & (S_{b1} and/or S_{b2})	$[0,-1,1]^\top$	$[0,-1]^\top$	$-0.25 < r_\alpha < 0.25$	$-1.25 < r_\beta < -0.75$	X	X	X
13	(S_{c3} and/or S_{c4}) & (S_{b3} and/or S_{b4})	$[0,1,1]^\top$	$[-1,0]^\top$	$-1.25 < r_\alpha < -0.75$	$-0.25 < r_\beta < 0.25$	N	P	P
14	(S_{b1} and/or S_{b2}) & (S_{a3} and/or S_{a4})	$[1,-1,0]^\top$	$[\sqrt{3}/2,-1/2]^\top$	$0.6 < r_\alpha < 1.1$	$-0.75 < r_\beta < -0.25$	X	X	X
15	(S_{b1} and/or S_{b2}) & (S_{c1} and/or S_{c2})	$[0,-1,-1]^\top$	$[1,0]^\top$	$0.75 < r_\alpha < 1.25$	$-0.25 < r_\beta < 0.25$	P	N	N
16	(S_{a3} and/or S_{a4}) & (S_{b3} and/or S_{b4})	$[1,1,0]^\top$	$[1/2,\sqrt{3}/2]^\top$	$0.25 < r_\alpha < 0.75$	$0.6 < r_\beta < 1.1$	P	P	N
17	(S_{a3} and/or S_{a4}) & (S_{c1} and/or S_{c2})	$[1,0,-1]^\top$	$[\sqrt{3}/2,1/2]^\top$	$0.6 < r_\alpha < 1.1$	$0.25 < r_\beta < 0.75$	X	X	X
18	(S_{c1} and/or S_{c2}) & (S_{b3} and/or S_{b4})	$[0,1,-1]^\top$	$[0,1]^\top$	$-0.25 < r_\alpha < 0.25$	$0.75 < r_\beta < 1.25$	X	X	X

X denotes an irrelevant condition.

A2: The output R - L filter is considered a balanced load for the NPC inverter.

A3: The switching frequency is high enough compared to the fundamental supply frequency so that the inverter output voltages u_{lz} are assumed continuous signals.

A4: The three-phase utility grid is considered a balanced and symmetrical supply system.

In this scenario, an average model is employed for observer design purposes in the model-based strategy for FDI. The NPC inverter system model is obtained by analysing the dynamic behaviour of the currents injected into the utility grid, and by employing a two-phase representation through Clarke's transformation

$$\boldsymbol{x}_{\alpha\beta} = \begin{bmatrix} x_\alpha \\ x_\beta \end{bmatrix} = \sqrt{\frac{2}{3}} \begin{bmatrix} 1 & -\frac{1}{2} & -\frac{1}{2} \\ 0 & \frac{\sqrt{3}}{2} & -\frac{\sqrt{3}}{2} \end{bmatrix} \begin{bmatrix} x_a \\ x_b \\ x_c \end{bmatrix} = \boldsymbol{T}\boldsymbol{x}_{abc}, \tag{1}$$

$$\Rightarrow \boldsymbol{x}_{abc} = \boldsymbol{T}_r^{-1}\boldsymbol{x}_{\alpha\beta}, \tag{2}$$

where $\boldsymbol{T} \in \mathbb{R}^{3\times 2}$ denotes Clarke's transformation matrix. An important property of the NPC inverter system model in $\alpha\beta$ coordinates is its decoupling condition over the dynamics of the line currents. Hence, by taking into account the above properties, the following decoupled model in state-space representation is obtained:

$$\begin{aligned} \dot{\boldsymbol{x}} &= \boldsymbol{A}\boldsymbol{x} + \boldsymbol{B}\boldsymbol{u} + \boldsymbol{D}\boldsymbol{v}, \\ \boldsymbol{y} &= \boldsymbol{C}\boldsymbol{x}, \end{aligned} \tag{3}$$

where $\boldsymbol{x} = \begin{bmatrix} i_\alpha & i_\beta \end{bmatrix}^\top$ represents the vector of currents injected into the utility grid; $\boldsymbol{u} = \begin{bmatrix} u_\alpha & u_\beta \end{bmatrix}^\top$ is the vector of AC output voltages generated by the NPC inverter; $\boldsymbol{v} = \begin{bmatrix} v_\alpha & v_\beta \end{bmatrix}^\top$ is the vector of grid voltages; $\boldsymbol{A} = -R/L \cdot \boldsymbol{I}_2$; $\boldsymbol{B} = 1/L \cdot \boldsymbol{I}_2$; $\boldsymbol{C} = \boldsymbol{I}_2$; and $\boldsymbol{D} = -1/L \cdot \boldsymbol{I}_2$. In the following section, the model described in (3) is employed for the synthesis of dedicated observers in the model-based FDI proposal.

3 Residual generation methodologies for OCF diagnosis

3.1 Actuator faults modelling

Once an OCF occurs, the effect of this fault is reflected on the performance and efficiency of the NPC inverter, which is directly associated with a reduction in the voltage gain. Under this consideration, and following the motivation in [20, 21], the OCFs in the inverter are modelled as actuator faults by using an additive structure [24]. Consequently, the resulting faulty actuator voltages are expressed as follows:

$$u_{lz}^f(t) = u_{lz}(t) + f_l(t), \quad l \in \{a,b,c\}; \tag{4}$$

where $\left(u_{az}^f, u_{bz}^f, u_{cz}^f\right)$ denote the faulty actuator voltages of the NPC inverter; (u_{az}, u_{bz}, u_{cz}) are the nominal output voltages; and (f_a, f_b, f_c) represent the induced faults in the output voltages of the inverter, where $f_a(t) = 0$, $f_b(t) = 0$, and $f_c(t) = 0$, $\forall t$ during a fault-free scenario.

When an OCF occurs in the lower switching devices of phase l, the inverter cannot supply the negative part of the output voltage u_{lz}. Consequently, the fault profile f_l will exhibit a positive direction, i.e. $f_l \geq 0$ after fault triggering. Meanwhile, when an OCF occurs in the upper switches (S_{l1} and/or S_{l2}) of phase l, now the inverter is not able to supply the positive state of the output voltage. Hence this condition leads to a negative profile in the induced fault, i.e. $f_l \leq 0$ after triggering. As a result, six possible directions in the profiles can be identified for single faults by considering a three-phase reference frame abc, and 12 more for simultaneous ones (see Table 1).

Following this context, after Clarke's transformation in (1), the effect associated with a faulty profile in the abc frame will be concurrently reflected along $\alpha\beta$-axes [20, 21]. Moreover, the additive perspective in (4) for the faulty actuator voltages in the abc frame is preserved in the mathematical model after the linear transformation $\boldsymbol{T}$ to the $\alpha\beta$ frame. Hence, the faulty actuator voltages in $\alpha\beta$ reference frame $\left(u_\alpha^f, u_\beta^f\right)$ are given by

$$u_m^f(t) = u_m(t) + f_m(t), \quad m \in \{\alpha, \beta\}. \tag{5}$$

On the other hand, in [25], the post-fault behaviour of the current trajectories under single and double OCF scenarios in a standard voltage source inverter (VSI) was analytically characterised by using Fourier series. In this analysis, the pattern described by the faulty current contains a DC term plus harmonic components of the fundamental and switching frequencies of the inverter. In fact, the DC component is a distinctive characteristic of the OCFs present in the inverter. Therefore, since the resulting fault profiles in the VSI are similar to the NPC inverter, the aforementioned principles are applied to the fault profiles induced in this study. Following this philosophy, the fault profiles f_m in $\alpha\beta$ frame are characterised by a DC term plus oscillatory components:

$$f_m(t) = f_{mo} + \Delta f_m(t), \quad m \in \{\alpha, \beta\}, \tag{6}$$

where $(f_{\alpha o}, f_{\beta o})$ denote the DC terms and $(\Delta f_\alpha(t), \Delta f_\beta(t))$ represent the oscillatory components. Furthermore in a practical scenario, due to the structure of the NPC inverter, the oscillatory components are bounded in magnitude, i.e. $\exists \Gamma_m > 0\, (m \in \{\alpha, \beta\})$ such that $|\Delta f_m(t)| \leq \Gamma_m \, \forall t$.

3.2 Fault directionality

In this study, the resulting fault directions are used for isolation purposes. In this regard, a unitary vector $\boldsymbol{f}_{abc} = \begin{bmatrix} \hat{f}_a & \hat{f}_b & \hat{f}_c \end{bmatrix}^{\mathrm{T}}$ is defined in the *abc* frame, where $\hat{f}_l (l \in \{a, b, c\})$ represents the normalised fault direction in phase *l*. In this way, $\hat{f}_l = -1$ denotes an OCF in the upper switches, and $\hat{f}_l = 1$ for the lower ones. Next, the resulting unitary vector $\boldsymbol{f}_{\alpha\beta} \in \mathbb{R}^2$ in the $\alpha\beta$ frame is

$$\boldsymbol{f}_{\alpha\beta} \triangleq \frac{\boldsymbol{T}\boldsymbol{f}_{abc}}{\| \boldsymbol{T}\boldsymbol{f}_{abc} \|}, \tag{7}$$

where $\boldsymbol{T}$ is Clarke's transformation matrix given in (1). Thus, from (7) and unitary vectors $\boldsymbol{f}_{abc}$ for each fault profile in the *abc* frame, Table 1 shows the corresponding fault directions $\boldsymbol{f}_{\alpha\beta}$ in $\alpha\beta$ coordinates associated with single and simultaneous OCFs scenarios in the NPC inverter. As a result, there is ambiguity in the $\alpha\beta$ frame for several conditions, i.e. for the pairs of classes (1,13), (2,15), (3,11), (4,9), (5,16) and (6,7), the resulting fault vector $\boldsymbol{f}_{\alpha\beta}$ is the same, as described in Table 1.

In this way, an FDI strategy focused just on identifying the fault directions $\boldsymbol{f}_{\alpha\beta}$ will not be able to isolate all studied cases, so this motivates the idea of pursuing a combined approach between a model-based scheme that estimates the fault directions, and a data processing algorithm that extracts fault signatures from the available measurements in the NPC inverter. Therefore, departing from the state-space model in (3) and the additive structures of the fault profiles in (5) and (6), sliding-mode PI observers are suggested to generate residuals to estimate the DC fault components $(f_{\alpha o}, f_{\beta o})$. Meanwhile, the mean values of the line currents are computed to identify new fault signatures to enlarge the set of identifiable OCFs.

3.3 Residual generation by model-based approach

As described earlier, a part of the FDI scheme for OCFs relies on a model-based approach through dynamic observer design. In the literature, several approaches have been proposed for system observation [26]. Among the existing dynamical structures for state observation, sliding-mode PI observers are widely used due to their characteristics of finite-time convergence, robustness, and capability to reject or estimate certain perturbations [27]. Consequently, the dynamic structure of a sliding-mode PI observer is suggested to reconstruct the states dynamics and generate an estimation of the DC fault profiles $\left(\hat{f}_\alpha, \hat{f}_\beta\right)$, such that a residual generator could be constructed. First, from (3), two decoupled scalar subsystems $(\Sigma_\alpha, \Sigma_\beta)$ can be obtained in a fault scenario

$$\Sigma_m: \begin{cases} \dot{x}_m = Ax_m + B(u_m + f_m) + Dv_m, \\ y_m = x_m, \quad m \in \{\alpha, \beta\} \end{cases} \tag{8}$$

where $A \triangleq -R/L$, $B \triangleq 1/L$, and $D \triangleq -1/L$. Next, the dynamics of the faulty subsystems in (8) are employed to build two observers for FDI purposes, whose structure is defined in the next proposition. A detailed proof of this result is described in the Appendix.

Proposition: The currents estimation $\left(\hat{i}_\alpha, \hat{i}_\beta\right) = \left(\hat{x}_\alpha, \hat{x}_\beta\right)$ and the DC fault profiles estimation $\left(\hat{f}_\alpha, \hat{f}_\beta\right)$ are obtained departing from the following structure of sliding-mode PI observers:

$$\begin{aligned} \dot{\hat{x}}_m &= A\hat{x}_m + B(u_m + \hat{f}_m) + Dv_m + G(x_m - \hat{x}_m) \\ &\quad + K\left|x_m - \hat{x}_m\right|^2 \operatorname{sgn}(x_m - \hat{x}_m), \\ \dot{\hat{f}}_m &= H(x_m - \hat{x}_m), \\ \hat{y}_m &= \hat{x}_m, \quad m \in \{\alpha, \beta\} \end{aligned} \tag{9}$$

where $G, K, H \in \mathbb{R}^+$ are the observer gains, and $\operatorname{sgn}(\cdot)$ denotes the sign function. With this observer, the state error trajectories $e_x = x_m - \hat{x}_m$ will converge in finite time to a neighbourhood of the origin, i.e. e_x converges to a ball

$$\Psi \triangleq \left\{ e_x \in \mathbb{R} : \left| e_x \right| \leq \left(\sqrt{\frac{\Gamma_m H}{Q} + \frac{1}{4}} - \frac{1}{2} \right) \right\}, \tag{10}$$

where the rate of convergence can be directly adjusted by gains G and K in (9) and $Q > 0$ is a positive parameter (see convergence proof in the Appendix).

From the previous result, the following properties are pointed out:

- The proposed observers in (9) require feedback information from the NPC inverter voltages (u_α, u_β), the grid voltages (v_α, v_β), and the line currents (i_α, i_β). In addition, as the NPC inverter is operating under a closed-loop system [22], then the inverter voltages (u_α, u_β) are immediately available.
- The dynamical structure of the observers is confirmed by a copy of each subsystem in (8) plus linear and non-linear correction terms, where for simplicity the gains (G, K, H) are common for both observers.
- The observers in (9) include an augmented state $\hat{f}_m$ to estimate the DC fault profiles by the integral correction term, where the gain $H \in \mathbb{R}^+$ affects the desired convergence rate of the estimation.
- From the proof in the Appendix (see (18) and (23)), by applying Barbalat's lemma, in the absence of the oscillatory component $\Delta f_m(t) = 0$ (i.e. $\Gamma_m = 0$), the fault profile estimation $\hat{f}_m$ approaches the DC component f_{mo} as $t \to \infty$. Also, from (18) and (23), in a free-fault scenario $(f_m = 0)$, asymptotic convergence of the state error e_x is guaranteed.
- Also, from the Appendix, the observer gains (G, K, H) can be tuned by the following guidelines: (i) $G \gg R/L$ to improve the linear damping in the error convergence; (ii) $K \ll G$ to avoid increasing the noise sensitivity by the quadratic error correction term, where $K \triangleq Q/P$ and $P, Q \in \mathbb{R}^+$; (iii) $H \gg 1$ to have a fast convergence of the fault profile estimations (for design purposes, we suggest to assign an initial value of $H \triangleq BP$, see (20) and (21)). Note that by selecting $Q > H$ and $G \gg R/L$, the neighbourhood for error convergence is always bounded even in the presence of parameter uncertainty of the resistor–inductor (R–L) filter (see (24)).

3.4 Fault signatures by data processing

In order to overcome the redundancy of the model-based scheme for concurrent OCFs, and to complement its information in the fault isolation stage, new fault signatures are computed departing from the line currents in the NPC inverter. As described in Section 3.1, a fault will stop the bidirectional current flow in the power converter, so the average line current over a fundamental period will not be zero any more. In this way, a positive or negative average value per line current will give an indication of a fault in the inverter leg and also of its directionality, as illustrated in [28] for a three-phase VSI. To quantify this condition and to provide a robust fault signature, an indicator function is applied to each line current

$$w_l(t) = \begin{cases} 0 & |i_l(t)| \leq I_{\text{TH}}, \\ \text{sgn}(i_l(t)) & \text{otherwise}, \end{cases} \quad l \in \{a, b, c\}, \tag{11}$$

where I_{TH} is a threshold to take into account measurement noise, and this value should be selected according to the specifications of the employed current sensors (signal-to-noise ratio and error tolerance properties). Next, a new diagnostic variable is computed by a moving average of $w_l(t)$ over the fundamental period T of the utility grid

$$W_l(t) = \frac{1}{T}\int_{t-T}^{t} w_l(t)\mathrm{d}t, \quad l \in \{a, b, c\}. \tag{12}$$

Therefore, the signals $(W_a(t), W_b(t), W_c(t))$ will be approximately zero in a fault-free case.

After a fault, these diagnostic variables will observe a transient and will reach a steady-state response in roughly one fundamental period T. In steady-state, the signal $|W_l(t)|$ will be almost 0.5 in the faulty phase, due to the asymmetric line current. Nonetheless, $|W_l(t)|$ can be >0.5 due to the induced unbalance in the DC-link after a fault, which produces a DC bias in the remaining currents. Therefore, the fault signatures $(\mathscr{D}_a(t), \mathscr{D}_b(t), \mathscr{D}_c(t))$ are computed by labelling the signals $W_l(t)$ as negative (N), positive (P) or zero (Z) by using a threshold of ± 0.4

$$\mathscr{D}_l(t) \triangleq \begin{cases} N & W_l(t) < -0.4, \\ Z & -0.4 \leq W_l(t) \leq 0.4, \\ P & W_l(t) > 0.4, \end{cases} \quad l \in \{a, b, c\}. \tag{13}$$

Consequently, the fault signatures in (13) will indicate the directionality of the line currents after a fault, and by using the estimated fault profiles in the model-based scheme, all the 18 fault classes described in Table 1 can be isolated. Nonetheless, the 18 fault classes denote pairs of upper or lower faulty switches in the NPC inverter. Hence a subsequent analysis of the instantaneous current in the faulty phase will let to isolate the specific OCF.

4 FDI scheme

First, from the sliding-mode PI observers in (9), a vector with the estimated fault profiles $\hat{\boldsymbol{f}}_{\alpha\beta} = \begin{bmatrix} \hat{f}_\alpha & \hat{f}_\beta \end{bmatrix}^\top$ is constructed in the $\alpha\beta$ frame. In addition, a normalisation step is performed for each component of the vector $\hat{\boldsymbol{f}}_{\alpha\beta}$, in order to obtain diagnostic variables that are independent of the operating point of the NPC inverter. In this way, two residuals (r_α, r_β) are formulated by considering the following expression:

$$r_m = \begin{cases} \dfrac{\hat{f}_m}{\| \hat{\boldsymbol{f}}_{\alpha\beta} \|} & \| \hat{\boldsymbol{f}}_{\alpha\beta} \| > J_{\text{TH}}, \\ 0 & \| \hat{\boldsymbol{f}}_{\alpha\beta} \| \leq J_{\text{TH}}, \end{cases} \tag{14}$$

where $m \in \{\alpha, \beta\}$, and J_{TH} is a threshold used to avoid singularities in (14) and to take into account measurement noise, as well as, oscillatory components induced by pulse-width modulation voltages in the NPC inverter. This threshold parameter J_{TH} can be defined by running the system under a free-fault scenario such that

$$J_{\text{TH}} = \max_{\text{nofault } \forall t, m} \left| \hat{f}_m(t) \right|. \tag{15}$$

Therefore, fault detection is accomplished if

$$\text{Decision} = \begin{cases} \text{Fault} & \| \boldsymbol{r}_{\alpha\beta} \| > 0, \\ \text{Nofault} & \| \boldsymbol{r}_{\alpha\beta} \| = 0, \end{cases} \tag{16}$$

where $\| \boldsymbol{r}_{\alpha\beta} \|$ represents the Euclidean norm of the residual vector $\boldsymbol{r}_{\alpha\beta} = \begin{bmatrix} r_\alpha & r_\beta \end{bmatrix}^\top$. Once a fault is detected, the fault isolation process is carried out by evaluating the direction in $\alpha\beta$ axes of the residuals (r_α, r_β) obtained from (14). Hence, since a normalisation process is applied to the fault profiles $\left(\hat{f}_\alpha, \hat{f}_\beta\right)$ that construct the residuals in (14), (r_α, r_β) will exhibit a directional pattern according to the orientation specified by the fault vector $\boldsymbol{f}_{\alpha\beta}$ in Table 1. However, due to measurement noise and the presence of oscillatory components in the estimated DC fault profiles, the residual directions are evaluated by selecting upper and lower thresholds to take into account the effect of the described perturbations. Consequently, the isolation process is performed by using the thresholds proposed in Table 1 for each fault scenario. Note that the suggested variation intervals are centred at the expected values for each fault direction and obtained by adding a deviation of ± 0.25.

As pointed out earlier, to overcome the ambiguity by just using the model-based FDI scheme, the fault signatures $(\mathscr{D}_a, \mathscr{D}_b, \mathscr{D}_c)$ in (13) are evaluated jointly with the residues in (14), as described in Table 1 to isolate the faulty pair of switches in the upper or lower legs of the NPC inverter. Nonetheless, by further processing of the line current, each specific faulty switch can be identified. As pointed out in [11], after an OCF in the upper switch S_{l_1} (see Fig. 1), there is still current flowing in the positive direction during the positive semi-cycle of the grid voltage v_{ln} (see upper plot in the first column of Fig. 1), since phase l is still connected to the midpoint point z of the DC-link by the diode D_{l_1} and power switch S_{l_2} by the induced unbalance due to the fault. This condition applies if the NPC inverter was initially transferring either active or reactive power to the grid. In fact, under a closed-loop control scheme [22], the controller will try to compensate this unbalance due to the fault, but the voltage at point z will still be different from zero allowing a small positive current flow after an OCF in S_{l_1}.

However, in the case of an OCF in S_{l_2} (see Fig. 1), there cannot be current flowing in the positive direction (see the upper plot in the second column of Fig. 2), since there is no possible connection to the point z in the DC-link. A similar analysis applies for the negative semi-cycle of the grid voltage v_{ln} in the case of OCFs in the lower switches (S_{l_3} and S_{l_4}), which indicates that for S_{l_4} there is still some negative current flow after a fault, but for S_{l_3}, there is not (see Fig. 2 lower plots). In summary, the decision rule for final fault isolation in l phase is given by an instantaneous evaluation of

$$\text{Isolated faulty switch} = \begin{cases} S_{l_1} & v_{ln} > 0 \ \& \ w_l = 1, \\ S_{l_2} & v_{ln} > 0 \ \& \ w_l \in \{0, -1\}, \\ S_{l_3} & v_{ln} < 0 \ \& \ w_l \in \{0, 1\}, \\ S_{l_4} & v_{ln} < 0 \ \& \ w_l = -1. \end{cases} \tag{17}$$

As a consequence, this line current behaviour allows to further isolate each faulty switch in the NPC inverter. Therefore, the FDI scheme proposed in the present work is able to identify 6×2 single OCFs (classes 1–6 in Table 1) and 12×4 simultaneous OCFs (classes 7–18 in Table 1) in the NPC inverter by a combined model-based and data processing approach. The overall flow diagram of the proposed FDI scheme is illustrated in Fig. 3.

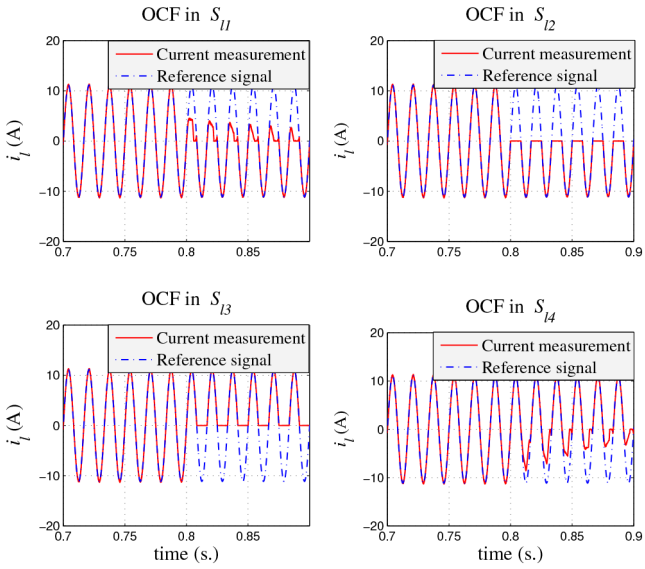

Fig. 2 *Current flow trajectory for an OCF in switches S_{l1}, S_{l2}, S_{l3}, and S_{l4}*

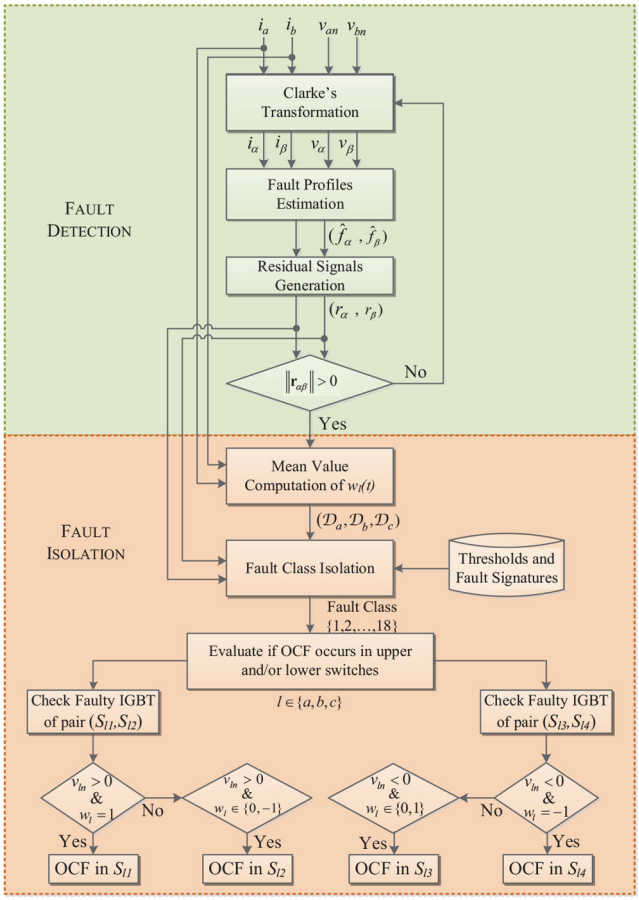

Fig. 3 *Flow chart of the proposed FDI scheme*

5 Experimental results

5.1 System setup

An experimental evaluation of the grid-connected NPC inverter is carried out for single and simultaneous faults in order to validate the FDI scheme suggested in this work. The experimental test bench is shown in Fig. 4. The parameters and design specifications used for the experiments are described in Table 2. The proposed observer gains were tuned by the guidelines described in Section 3.3 to provide fast error convergence and good noise robustness: $G = 2500$, $H = 200$, and $K = 1$. In addition, only active power is injected into the utility grid with a reference value of $P_{\text{ref}} = 300\,\text{W}$ per phase. The threshold values in (11) and (14) for the indicator and residual signals, respectively, were set to $I_{\text{TH}} = 0.16$ and $J_{\text{TH}} = 6$ by monitoring the time-pattern of these signals under a no-fault scenario, as described in Sections 3 and 4.

The NPC inverter is working in closed-loop following the model-based control methodology in [29]. First, a current tracking-loop was designed to transfer active power to the utility grid. The control law follows a proportional structure plus a bank of resonant filters to provide harmonic compensation and guarantee to track of the line currents towards the desired reference signal. Also, an outer-control loop was implemented to provide balance in the DC-link capacitor voltages by a proportional scheme with limited bandwidth. The proportional gain of the current tracking-loop was selected as $k_p = 45$, and for the balancing loop as $k_2 = 0.17$ and $\tau_2 = 0.001$. For this evaluation, the bank of resonant filters was not activated in order to evaluate the robustness of our FDI scheme under noise and harmonic distortion in the line currents.

5.2 Fault scenarios

To illustrate the diagnosis capability of our FDI proposal, we show the next experimental responses of single and simultaneous fault scenarios:

- *Case A*: an OCF occurs ($t = 24.1843\,\text{s}$) at phase a on the upper switch S_{a1} (fault class 1, see Table 1).
- *Case B*: simultaneous OCFs occur ($t = 15.6791\,\text{s}$) at phase a on the upper switch S_{a2}, and at phase b on the lower switch S_{b4} (fault class 8, see Table 1).

The results for *Case A* are shown in Figs. 5*a* and *b*. Initially, the performance of the current tracking controller can be observed in Fig. 5*a*. The experimental results show that the injected current i_l follows the reference signal i_l^*. Once the OCF is triggered at $t = 24.1843\,\text{s}$, the connection with the positive DC-link is not allowed at phase a, although there is some positive current flowing by diode D_{la} and switch S_{a2}. As a result, current i_a is flowing only in the negative direction (see Fig. 5*a*), and the remaining currents (i_b, i_c) adjust their magnitudes to maintain its balance property $(i_a + i_b + i_c = 0)$. Also, after fault triggering, the residuals (r_α, r_β) promptly indicate the presence of a fault (see the second panel in Fig. 5*b*) showing good robustness despite the harmonic distortion and the measurement noise in the line currents. Consequently, the fault alarm is triggered quickly, and fault detection is achieved at $t = 24.1886\,\text{s}$ (see the top panel in Fig. 5*b*). Therefore, after the fault triggering the OCF detection is achieved in just 4.3 ms.

Next by analysing the residual directionality defined in Table 1, since the residuals (r_α, r_β) enter the intervals $-1.25 < r_\alpha < -0.75$ and $-0.25 < r_\beta < 0.25$ (see the last panel in Fig. 5*b*), there is ambiguity in the model-based FDI scheme since classes 1 and 13 could be either identified. Hence, the information about the data processing strategy is taken into account. After this initial decision by the model-based algorithm and roughly one period of the fundamental frequency (16 ms), the diagnostic variables (W_a, W_b, W_c) reach a steady-state value (see the third panel in Fig. 5*b*), so the following fault signature in (13) is obtained $(\mathcal{D}_a, \mathcal{D}_b, \mathcal{D}_c) = (N, Z, Z)$. Therefore by Table 1, an OCF in the upper switches of phase a (S_{a1} and/or S_{a2}) is finally isolated. Finally, from (17) and the resulting line currents after a fault in Fig. 5*a*, a fault in the switch S_{a1} is concluded since for the positive semi-cycle ($i_a^* > 0$ which is proportional to v_{an}), the indicator signal $w_a(t)$ in (11) takes the value 1.

The experimental results for *Case B* are illustrated in Figs. 6*a* and *b*. After fault triggering at $t = 15.6791\,s$, phase a cannot be connected to the positive DC-link. Meanwhile, the connection with the negative DC-link is not allowed at phase b, although for this case there is some positive current flowing by diode D_{2b} and switch S_{b3}. Owing to the simultaneous fault condition, the current flow in phases a and b present an asymmetrical alternating shape, and i_c adjusts its trajectory (see Fig. 6*b*). As a result, residuals (r_α, r_β) quickly enter the intervals $-1.1 < r_\alpha < -0.6$ and $0.25 < r_\beta < 0.75$

(see the second panel in Fig. 6*b*). Next, the fault alarm is triggered indicating the presence of a fault, and as a consequence, fault detection is achieved in just 2.6 ms (at $t = 15.6817$ s, see the top panel in Fig. 6*b*).

In this case, fault isolation is performed by just evaluating the residual directions since there is no ambiguity in the model-based FDI scheme, i.e. FDI is achieved jointly. Hence according to Table 1, we observed simultaneous OCFs in the upper switches of phase a (S_{a1} and/or S_{a2}), and the lower switches of phase b (S_{b3} and/or S_{b4}). Furthermore, from (17) and the resulting time-pattern of the line currents after a fault in Fig. 6*a*, an OCF in the switch S_{a2} is concluded since for the positive semi-cycle ($i_a^* > 0$), the indicator signal $w_a(t)$ in (11) only takes the values $\{0, -1\}$. Furthermore, also a fault in the switch S_{b4} is diagnosed since the indicator signal $w_c(t)$ in (11) takes the value -1 for the negative semi-cycle ($i_c^* < 0$).

Finally, the robustness of the diagnostic variables was evaluated against changes in the operating point of the NPC inverter in closed-loop control operation. The experimental results for *Case A* and *Case B* are shown in Figs. 7*a* and *b*. The results for *Case A* in Fig. 7*a* (first panel) illustrate the changes in the operating point of the NPC inverter. For this case, the active power injected into the grid increased at $t = 14.40$ s from 100 to 200 W. In addition, a different transient response in the active power is visualised at $t = 19.17$ s. Here, the reference of the active power was updated to

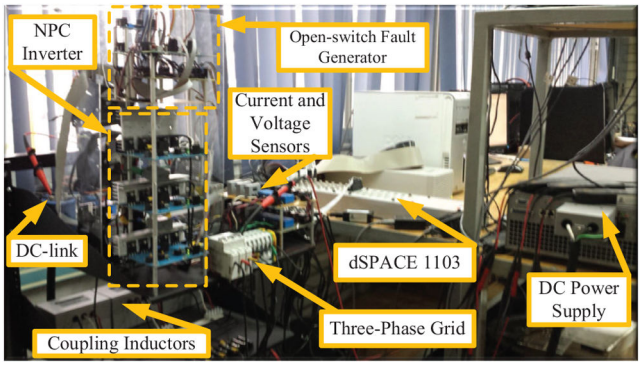

Fig. 4 *Experimental prototype of the grid-connected NPC inverter*

Table 2 Parameters of the experimental three-phase NPC inverter

Parameter	Value
grid line voltage per phase	$v_{ln} = 127\ V_{\rm rms}\ \forall n \in \{a, b, c\}$
fundamental period	$T = 1/60$ s
resistive looses	$R = 0.1\ \Omega$
inductive filter	$L = 5$ mH
DC-link voltage	$V_{\rm dc} = 220$ V
DC-link capacitors	$C = 2200\ \mu$F

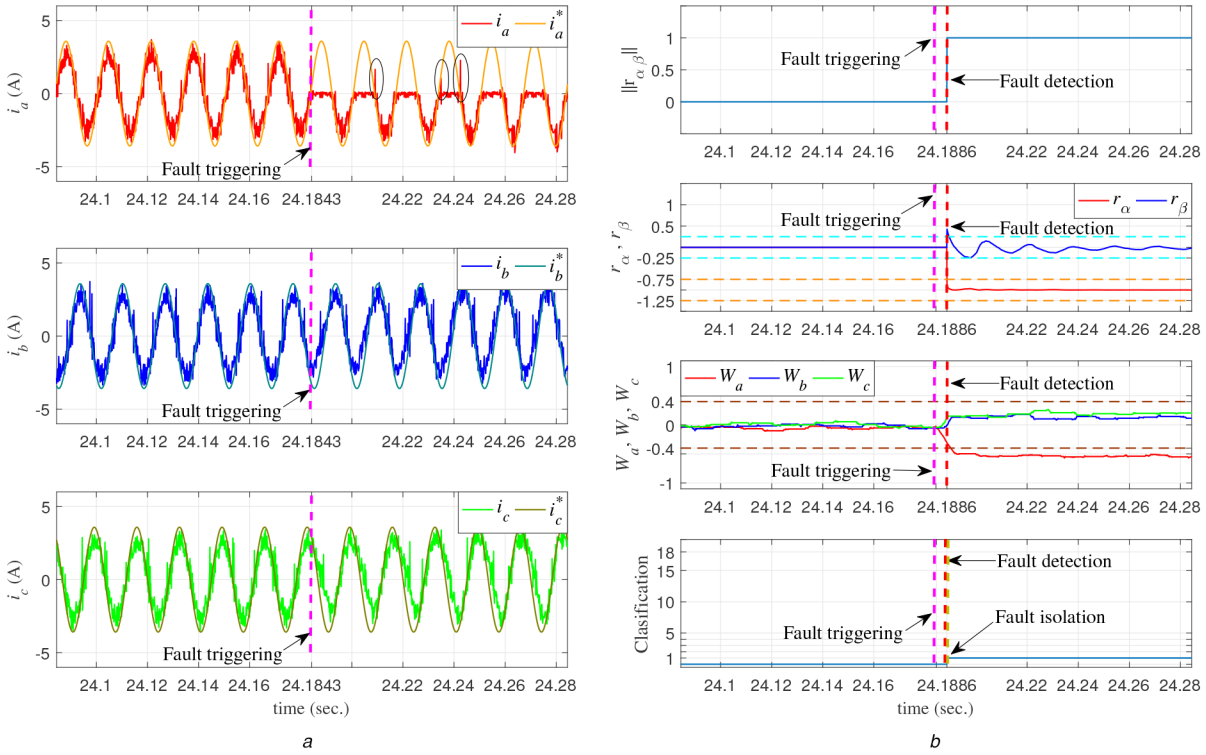

Fig. 5 *Experimental results for Case A*

(a) Experimental results for *Case A*: line current measurements (i_a, i_b, i_c) in the NPC inverter and current references for closed-loop control (i_a^*, i_b^*, i_c^*), ***(b)*** Experimental results for *Case A*: (first) norm of vector residual $\| \boldsymbol{r}_{\alpha\beta} \|$, (second) residuals (r_α, r_β), (third) fault signatures (W_a, W_b, W_c), (fourth) classification result

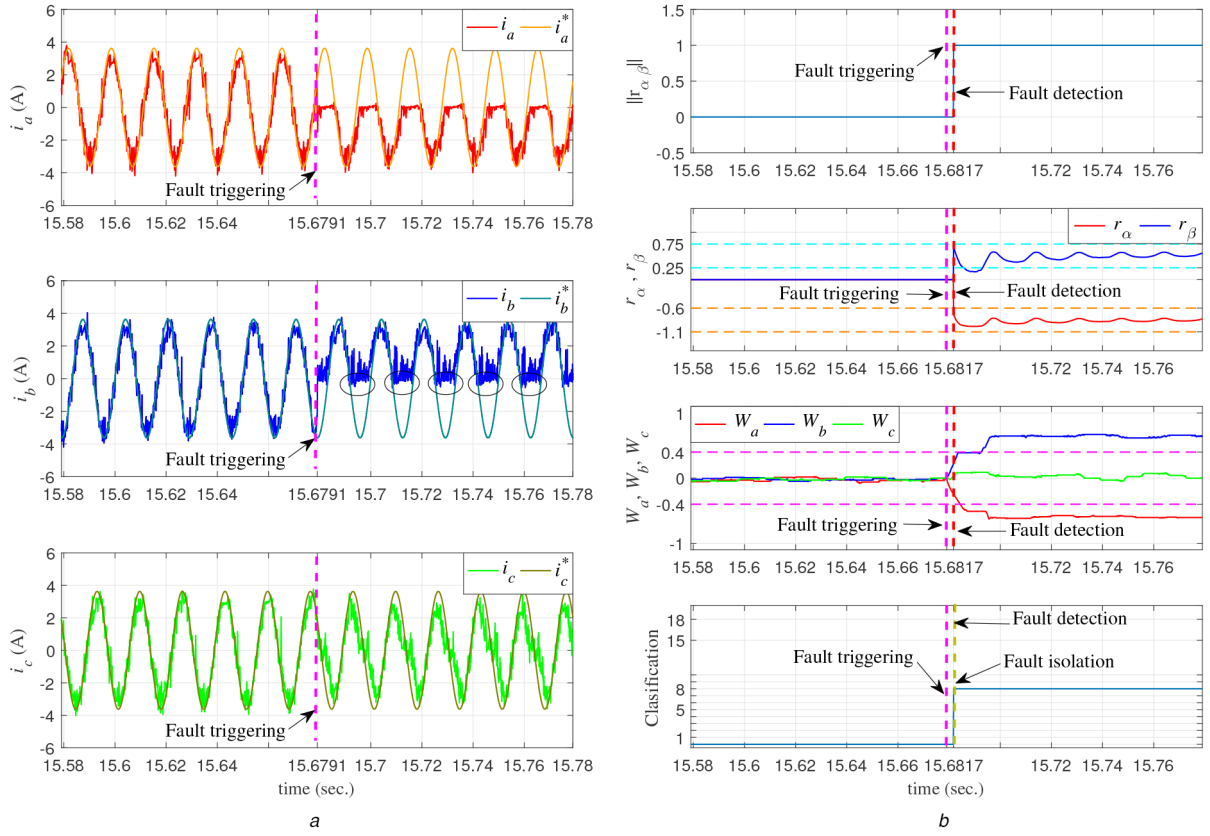

Fig. 6 *Experimental results for Case B*

(a) Experimental results for *Case B*: line current measurements (i_a, i_b, i_c) in the NPC inverter and current references for closed-loop control (i_a^*, i_b^*, i_c^*), ***(b)*** Experimental results for *Case B*: (first) norm of vector residual $\| \boldsymbol{r}_{\alpha\beta} \|$, (second) residuals (r_α, r_β), (third) fault signatures (W_a, W_b, W_c), (fourth) classification result

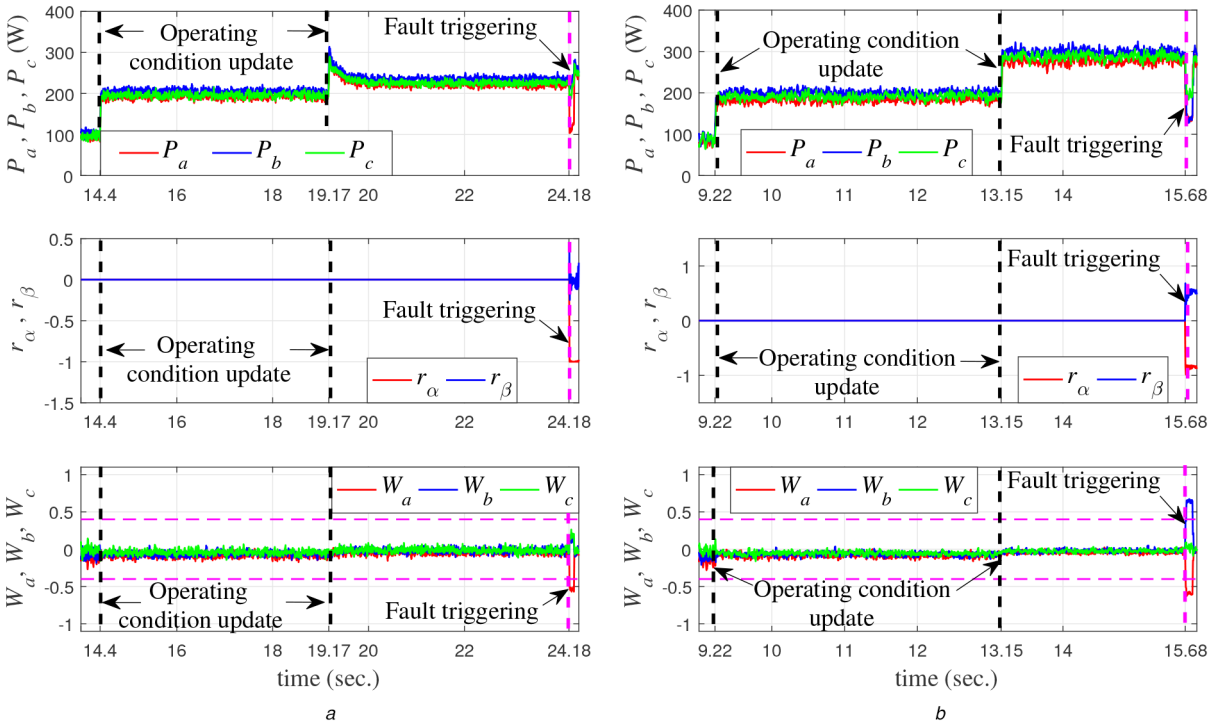

Fig. 7 *Experimental results for Case A and Case B with changes in the operating point of the NPC inverter*

(a) Experimental results for *Case A*: (first) active power (P_a, P_b, P_c) transferred to the grid, (second) residuals (r_α, r_β), (third) fault signatures (W_a, W_b, W_c), ***(b)*** Experimental results for *Case B*: (first) active power (P_a, P_b, P_c) transferred to the grid, (second) residuals (r_α, r_β), (third) fault signatures (W_a, W_b, W_c)

300 W (per phase); nonetheless, the transferred active power did not reach the desired value, since the current supplied by the DC power source was limited to emulate a decrease in the maximum power point of the PV array. Hence the diagnostic variables were not affected by the change in the operating point of the NPC inverter, as can be seen in the second and third panels of Fig. 7*a*.

Next, after the OCF was triggered at $t \simeq 24.18$ s, the magnitude of the residuals (r_α, r_β) and (W_a, W_b, W_c) indicated the presence of a fault condition. Similarly, the simultaneous OCF scenario described in *Case B* was evaluated by changing the operating point of the inverter at $t = 9.22$ s, and $t = 13.15$ s (see Fig. 7*b*). Once

more, the diagnostic variables (r_α, r_β) and (W_a, W_b, W_c) were not affected by the changes in the operating point of the NPC inverter.

Further experimental results with more single and simultaneous faults were successfully detected and isolated, but they are not presented by space limitations. Nonetheless, the results reported in this study show that our FDI proposal is able to diagnose accurately single and simultaneous faults by using common current and voltage measurements, even under a closed-loop control operation. One important feature is that fault isolation in our test was in the order or lower than a fundamental period of the grid frequency.

5.3 Comparison with state-of-the-art algorithms

The proposed FDI algorithm was compared against three previous results, which have addressed OCFs in NPC inverters, which have used current measurements to generate residuals for the FDI scheme. The first approach is related to the methodology proposed in [9], meanwhile, the second FDI algorithm is the scheme presented in [11], and the third one is about a recent proposal reported in [17]. Owing to the space limitations, just *Case A* was considered for the comparison with the other FDI schemes. The results for the FDI scheme proposed in [9] are presented in the first and second panel of Fig. 8. After the OCF is triggered at $t = 24.1843$ s, the radius of the current pattern indicated the presence of a fault condition (see the first panel of Fig. 8). In addition, the time pattern of the instantaneous current vector phase-angle also modifies its trajectory (see the second panel of Fig. 8). Nevertheless, due to the harmonic contamination and measurement noise, the threshold selection for fault detection purposes is considered as a difficult task, as observed in Fig. 7. Another drawback of the FDI scheme presented in [9] is its sensibility to abrupt changes in the operating point of NPC inverter. In the absence of a normalisation process in the FDI scheme proposed by Choi *et al*. [9], transient response is expected in the radius of the current pattern. Consequently, a false alarm could be triggered as the radius of the current pattern will increase its value during a short period of time.

Now, the experimental results for the FDI scheme proposed in [11] are shown in the third panel of Fig. 8. In this case, the thresholds values $I^{\text{th}}_{\text{pos}} = 0.15$ pu, $I^{\text{th}}_{\text{neg}} = -0.15$ pu, $I^{\text{th}}_{\text{pos}_{\text{av}}} = 0.1$ pu, $I^{\text{th}}_{\text{neg}_{\text{av}}} = -0.1$ pu, and $I^{\text{th}}_{s_{\text{av}}n} = 0.1$ pu proposed in [11] were considered in the evaluation. Once the OCF is triggered at $t = 24.1843$ s, the magnitude of the residuals change its value to $d_a = 1$ and $e_a = 0$. As a result, FDI $d_a = 1$ and $e_a = 0$ achieved at $t = 24.1895$ s, and the trajectories of the residuals (d_a, e_a, f_a) allowed to identify the faulty IGBT pair as (S_{a1}, S_{a2}). Nonetheless, the diagnostic variable f_a in [11] is affected by the harmonic contamination and the noise in the current measurements (see the third panel of Fig. 8). Finally, the experimental results for the FDI scheme proposed in [17] are shown in the fourth panel of Fig. 8. In this case, the FDI can be carried out in less than a fundamental period (16.6 ms), which is similar to the results obtained in our FDI proposal. Nonetheless, the algorithm presented in [17] is able to diagnose only 6 × 2 single OCF scenarios.

Overall, the results of comparing our FDI scheme with the algorithms suggested in [9, 11, 17] is shown in Table 3. First, the algorithm presented in [11] showed sensitivity to measurement noise in the residual generation process. On the contrary, our proposal is robust to this condition, but also able to achieve FDI in less than one fundamental period. Meanwhile, the performance of the methodology proposed in [9] could have false alarms during the fault detection step at operating condition updates. Moreover, this scheme requires at least two fundamental periods to identify the faulty switch, which could be a limitation of the isolation scheme. Finally, the FDI algorithm suggested in [17] shown a similar performance as ours in terms of FDI time. However, our proposal is able to diagnose a larger set of single and simultaneous OCF scenarios.

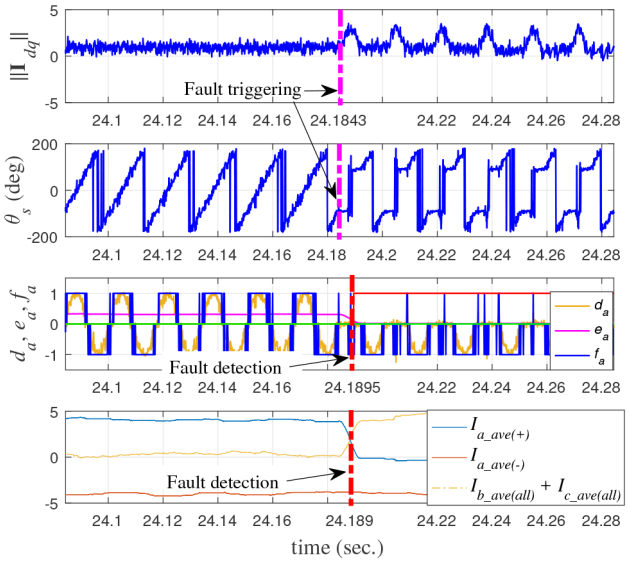

Fig. 8 *Experimental results for the comparison of the proposed FDI scheme with state-of -the-art algorithms with state-of -the-art algorithms [9], [11] and [17]*

Table 3 Comparison of the proposed FDI scheme with State-of-the-art algorithms

Reference	System	Measurements	Types of fault	Fault diagnosis capability	Detection time	Isolation time
proposed FDI scheme	grid-connected	phase currents and grid voltages	OCF in switches	6 × 2 single OCF and 12 × 4 simultaneous OCF	<16.66 ms	<16.66 ms
[9]	grid-connected	phase currents	OCF in switches	6 × 2 single OCF	<16.66 ms	>16.66 ms & <33.22 ms
[11]	AC motor drive	phase currents	OCF in switches	6×2 single OCF	<16.66 ms	<16.66 ms
[17]	grid-connected	phase currents	OCF in switches and clamping diodes	6 × 2 single OCF and 3 × 2 OCF clamping diodes	<16.66 ms	<16.66 ms

6 Final remarks

In this work, we addressed the problem of OCF diagnosis in grid-connected NPC inverters by using just the feedback information of line currents and grid voltages. For this purpose, a combined model-based and data processing approach was proposed to detect and isolate single and simultaneous OCFs. In the model-based FDI scheme, a bank of sliding-mode PI observers was designed to estimate the DC components of the fault profiles, which inherits the robustness to parametric uncertainty and noise of a variable-structure design. In this study, we prove analytically the convergence of the observers to a neighbourhood of the origin, whose size depends on the amplitude of the oscillating component of the fault profile. Meanwhile, the data processing FDI scheme employs the average line currents to generate extra fault signatures, where the final isolation of the faulty switch considers the instantaneous evaluation of the line currents. This combined process only requires typical measurements in the NPC inverter usually used in closed-loop control. Our experimental validation and comparison of the FDI scheme under single and simultaneous faults indicate that the combined FDI methodology is jointly robust to noise and disturbances, and also capable of promptly detecting and isolating the faulty switch in the inverter leg. A future work of this application relies on the proposal of a fault tolerant control strategy for the grid-connected NPC system; then, by departing from the proposed fault tolerant control strategy, we will estimate the reliability of the inverter by considering the FDI algorithm proposed in this study.

7 Acknowledgments

This research work was partially supported by a grant of Universidad Autónoma de San Luis Potosí (C18-FAI-05-49.49), and CONACyT (CB-255729-2016).

8 References

[1] International Energy Agency: '*World energy outlook 2017*' (OECD Publishing, IEA, Paris, 2017)
[2] International Energy Agency: 'Trends 2017 in photovoltaic applications', in '*Survey report of selected IEA countries between 1992 and 2016*' Report IEA PVPC T1-32:2017, (IEA Photovoltaic Power Systems Programme, Switzerland, 2017, 22nd edn.), pp. 1–80
[3] Kouro, S., Leon, J.I., Vinnikov, D., *et al.*: 'Grid-connected photovoltaic systems: an overview of recent research and emerging PV converter technology', *IEEE Ind. Electron. Mag.*, 2015, **9**, (1), pp. 47–61
[4] Petrone, G., Teodorescu, R., Veerachary, M., *et al.*: 'Reliability issues in photovoltaic power processing systems', *IEEE Trans. Ind. Electron.*, 2008, **55**, (7), pp. 2569–2580
[5] Wang, H., Liserre, M., Blaabjerg, F.: 'Toward reliable power electronics: challenges, design tools, and opportunities', *IEEE Ind. Electron. Mag.*, 2013, **7**, (2), pp. 17–26
[6] Ceballos, S., Pou, J., Robles, E., *et al.*: 'Three-level converter topologies with switch breakdown fault-tolerance capability', *IEEE Trans. Ind. Electron.*, 2008, **55**, (3), pp. 982–995
[7] Alavi, O., Hooshmand, A., Shamlou, S.: 'A comparative reliability study of three fundamental multilevel inverters using two different approaches', *Electronics*, 2016, **5**, (18), pp. 1–18
[8] Mirafzal, B.: 'Survey of fault-tolerance techniques for three-phase voltage source inverters', *IEEE Trans. Ind. Electron.*, 2014, **61**, (10), pp. 5192–5202
[9] Choi, U.M., Jeong, H.G., Lee, K.B., *et al.*: 'Method for detecting an open-switch fault in a grid-connected NPC inverter system', *IEEE Trans. Power Electron.*, 2012, **27**, (6), pp. 2726–2739
[10] Lee, J.S., Lee, K.B., Blaabjerg, F.: 'Open-switch fault detection method of a back-to-back converter using NPC topology for wind turbine systems', *IEEE Trans. Ind. Appl.*, 2015, **51**, (1), pp. 325–335
[11] Mendes, A.M.S., Abadi, M.B., Cruz, S.M.A.: 'Fault diagnostic algorithm for the three-level neutral point clamped AC motor drives, based on the average current park's vector', *IET Power Electron.*, 2014, **7**, (5), pp. 1127–1137
[12] Rodríguez-Blanco, M.A., Vázquez-Pérez, A., Hernández-González, L., *et al.*: 'Fault detection for IGBT using adaptive thresholds during the turn-on transient', *IEEE Trans. Ind. Electron.*, 2015, **62**, (3), pp. 1975–1983
[13] Jlassi, I., Estima, J.O., Khil, S.K.E., *et al.*: 'Multiple open-circuit faults diagnosis in back-to-back converters of PMSG drives for wind turbine systems', *IEEE Trans. Power Electron.*, 2014, **30**, (5), pp. 2689–2702
[14] Lee, J.S., Lee, K.B.: 'Open-switch fault tolerance control for a three-level NPC/T-type rectifier in wind turbine systems', *IEEE Trans. Ind. Electron.*, 2015, **62**, (2), pp. 1012–1021
[15] Caseiro, L.M., Mendes, A.M.S.: 'Real time IGBT open-circuit fault diagnosis in three-level neutral-point-clamped voltage-source rectifiers based on instant voltage error', *IEEE Trans. Ind. Electron.*, 2015, **62**, (3), pp. 1669–1678
[16] Abadi, M.B., Mendes, A.M.S., Cruz, S.G.A.: 'Method to diagnose open-circuit faults in active power switches', *IET Electr. Power Appl.*, 2016, **10**, (7), pp. 623–632
[17] Choi, U.M., Lee, J.S., Blaabjerg, F., *et al.*: 'Open-circuit fault diagnosis and fault-tolerant control for a grid-connected NPC inverter', *IEEE Trans. Power Electron.*, 2016, **31**, (10), pp. 7234–7247
[18] Goncalves, P.F.C., Cruz, S.M.A., Abadi, M.B., *et al.*: 'Fault-tolerant predictive power control of a DFIG for wind energy applications', *IET Electr. Power Appl.*, 2017, **11**, (6), pp. 969–980
[19] Abdelghani, A.B.B., Abdelghani, H.B., Richardeau, F., *et al.* 'Versatile three-level FC-NPC converter with high fault-tolerance capabilities: switch fault detection and isolation and safe postfault operation', *IET Electr. Power Appl.*, 2017, **11**, (6), pp. 969–980
[20] Campos-Delgado, D.U., Espinoza-Trejo, D.R.: 'An observed-based diagnosis scheme for single and simultaneous open-switch faults in induction motor drives', *IEEE Trans. Ind. Electron.*, 2010, **58**, (2), pp. 671–679
[21] Espinoza-Trejo, D.R., Campos-Delgado, D.U., Bárcenas, E., *et al.*: 'Robust fault diagnosis scheme for open-circuit faults in voltage source inverters feeding induction motors by using non-linear proportional-integral observers', *IET Power Electron.*, 2011, **5**, (7), pp. 1204–1216
[22] Rodriguez, J., Bernet, S., Steimer, P.K., *et al.*: 'A survey on neutral-point-clamped inverters', *IEEE Trans. Ind. Electron.*, 2010, **57**, (7), pp. 2219–2230
[23] Escobar, G., Leyva-Ramos, J., Carrasco, J.M., *et al.*: 'Modeling of a three level converter used in a synchronous rectifier application'. Proc. 365th Annual IEEE Power Electronics Specialist Conf., PESC'04, Aachen Germany, 2004, pp. 4306–4311
[24] Campos-Delgado, D.U., Espinoza-Trejo, D.R., Palacios, E.: 'Fault-tolerant control in variable speed drives: a survey', *IET Electr. Power Appl.*, 2008, **2**, (2), pp. 121–134
[25] Campos-Delgado, D.U., Pecina-Sánchez, J.A., Espinoza-Trejo, D.R., *et al.*: 'Diagnosis of open switch faults in variable speed drives by stator current analysis and pattern recognition', *IET Electr. Power Appl.*, 2013, **7**, (6), pp. 509–522
[26] Isermann, R.: '*Fault-diagnosis systems: an introduction from fault detection to fault tolerance*' (Springer-Verlag, Germany, 2006)
[27] Perruquetti, W., Barbot, J.P.: '*Sliding mode control in engineering*' (Marcel Dekker, Inc., New York, NY, USA, 2002)
[28] Sleszynski, W., Nieznanski, J., Cichowski, A.: 'Open-transistor fault diagnostics in voltage-source inverters by analyzing the load currents', *IEEE Trans. Ind. Electron.*, 2009, **56**, (11), pp. 4681–4688
[29] Valdez-Fernandez, A.A., Martínez-Rodríguez, P.R., Escobar, G., *et al.*: 'A model-based controller for the cascade H-bridge multilevel converter used as a shunt active filter', *IEEE Trans. Ind. Electron.*, 2013, **60**, (11), pp. 5019–5028

8 Appendix

Convergence proof: First, the estimation errors vector is defined as $e_x = x_m - \hat{x}_m$ and $e_f = f_{mo} - \hat{f}_m$ for $m \in \{\alpha, \beta\}$. Thus, from systems in (8) and (9), the time derivative along the error dynamics leads to

$$\begin{aligned} \dot{e}_x &= A_o e_x + B e_f + B\Delta f_m - K\left|e_x\right|^2 \mathrm{sgn}(e_x), \\ \dot{e}_f &= -H e_x, \end{aligned} \tag{18}$$

where $A_o \triangleq (A - G) \in \mathbb{R}^-$. Next, the following Lyapunov function is proposed to prove error convergence:

$$V = \frac{P}{2}e_x^2 + \frac{1}{2}e_f^2 \tag{19}$$

where $P \in \mathbb{R}^+$. Then, by considering the error dynamics in (18), the time derivative along the Lyapunov function V leads to

$$\begin{aligned} \dot{V} = {} & A_o P \mathrm{e}_x^2 + (BP - H)\mathrm{e}_f \mathrm{e}_x + \Delta f_m BP e_x \\ & - PK\mathrm{e}_x\left|\mathrm{e}_x\right|^2 \mathrm{sgn}(e_x). \end{aligned} \tag{20}$$

As a next step, for design purposes, we assign $H \triangleq BP$ and $K \triangleq Q/P$, and considering the fact that P satisfies the scalar Lyapunov equation $PA_o = -Q$ for $Q \in \mathbb{R}^+$ since $A_o < 0$, we obtain

$$\dot{V} = -Q\mathrm{e}_x^2 + H\Delta f_m \mathrm{e}_x - Q\mathrm{e}_x\left|\mathrm{e}_x\right|^2 \mathrm{sgn}(e_x). \tag{21}$$

Then, by recalling the bound on the oscillatory components of the fault profiles $|\Delta f_m(t)| \leq \Gamma_m < \infty$, the following inequality is deduced:

$$\Delta f_m H e_x \le \Gamma_m H |e_x| \quad \forall t\,. \tag{22}$$

Furthermore, due to the nature of the sign function, for any $x \in \mathbb{R}$, we have that $x = |x|\mathrm{sgn}(x)$. As a result, from the above properties and by using (22), the following upper bound on the time derivative of V is finally derived

$$\dot{V} \le -|e_x|\left(Q|e_x| + Q|e_x|^2 - \Gamma_m H\right). \tag{23}$$

Therefore, we have a negative definite derivative $\dot{V} < 0$ if

$$\begin{aligned} &\left|\mathrm{e}_x\right| + \left|\mathrm{e}_x\right|^2 > \frac{\Gamma_m H}{Q}, \\ &\Rightarrow |\mathrm{e}_x| > E_{\max}, \end{aligned} \tag{24}$$

where $E_{\max} \triangleq \sqrt{\frac{\Gamma_m H}{Q} + \frac{1}{4}} - \frac{1}{2} > 0$ defines the size of the neighbourhood for error convergence. Hence, the error is always bounded for the proposed observer in (9) in the case of a fault, and the convergence ball defined in (10) is deduced. □